Eleventh International Conference on Computational Fluid Dynamics (ICCFD11), Maui, Hawaii, July 11-15, 2022

ICCFD11-2022-1201

Ray tracing methodology for jet noise prediction

T. Shanbhag*, B. Y. Zhou**, C. R. S. Ilário*** and J. J. Alonso*
Corresponding author: tejals@stanford.edu

* Stanford University, USA
** University of Bristol, UK
*** EMBRAER S.A., Brazil.

Abstract: A computational aeroacoustics method based on Lighthill's analogy and geometrical acoustics is presented to calculate the noise arising from the mixing of subsonic turbulent jets. Both the source model and the far field propagation model use information obtained from a standard RANS $k-\epsilon$ simulation of the jet flow. The propagation model, which accounts for the effects of sound refraction, is based on a ray tracing methodology. This implementation makes very few simplifying assumptions about the flow field geometry, allowing this method to be applied to complicated nozzle configurations that result in inherently three-dimensional propagation effects. We apply this method to compute far field acoustic predictions for the Go4Hybrid round jet test case at $M = 0.9$. The computed spectra show good agreement with experimental measurements at various polar angles.

Keywords: Aeroacoustics, Jet Noise, Geometrical Acoustics, Lighthill's Analogy.

1 Introduction

As projections for the yearly growth in air traffic remain high, and urban populations continue to undergo rapid expansion, there is now a regulatory demand for significant reductions in the noise emitted by civil and military aircraft. Jet mixing noise is one of the major components of aircraft noise overall, particularly during take-off. Consequently, the reliable and computationally efficient calculation of jet noise has received considerable research interest in recent years. Significant jet noise reductions have hitherto been achieved by the increase of engine bypass ratios. Experimental studies have highlighted a number of promising design concepts with potential to achieve further reductions, such as asymmetric, beveled and chevron nozzles. These designs introduce geometrical complexity and inherently three-dimensional flow features - therefore, acoustic prediction tools with sufficient robustness to account for these features are required.

The approaches to numerical prediction of jet mixing noise are widely varied in cost and fidelity, spanning from empirical database interpolation to expensive FWH calculations reliant on LES or DNS data. In the context of design optimization, where repeated aeroacoustic evaluations of a flow field are required, it is highly desirable to develop a method that minimizes computational time and expense while retaining the necessary accuracy. Hybrid methodologies based on RANS simulations of the jet flow conditions are widely recognized as an alternative well suited to this purpose. These methods post-process mean flow quantities available from RANS calculations (time-averaged velocities, pressure, turbulent kinetic energy etc.) to construct models representing the turbulent correlation functions that appear in the source term of Lighthill's equation.

Early examples of this method type were presented by Balsa and Gliebe [1], who modeled the acoustic sources based on analytic representations of the mean flow. The Mani-Gliebe-Balsa-Khavaran (MGBK) method [2]builds upon this approach, replacing the use of analytic fits with a numerical $k-\epsilon$ turbulence solution. In this method, Lilley's equation is solved for a convecting source emitting a single frequency using the high frequency Green's function for an axisymmetric jet. Further exploration of acoustic analogy based methods was conducted by Tam and Auriault [3], whose proposed framework used an analogy between molecular and turbulent pressures to derive a form for the two-point correlations, and Morris and Farassat

[4], who showed that such a 'kinetic theory' approach is equivalent to the standard Goldstein acoustic analogy assuming a consistent form for the source term and Green's function are used. Other efforts to model the two point correlations on the basis of RANS quantities have focused on accurately capturing the characteristic turbulent length and time scales at different locations in the jet flow. Self and Azarpeyvand [5] [6] demonstrated the importance of accounting for frequency dependence in these scales when modeling turbulent statistics for acoustic calculations. These authors have also shown that inclusion of time scales based on different turbulent mechanisms, such as dissipation, production and energy transfer, results in significantly more accurate predictions overall, and in particular at low and high frequencies.

In this paper, we apply a source model based on Lighthill's acoustic analogy. The resulting far field SPL predictions show good agreement with experimental data at a polar angle of 90^o. In order to handle far field propagation, and incorporate the effects of sound refraction by the mean flow field, we apply a geometrical acoustics method. This ray tracing approach, demonstrated by Ilario et al. [7], interpolates flow field variables from a RANS simulation to integrate along the path of many rays from numerically distributed source locations to the far field observer locations. We demonstrate that coupling the source modeling approach with this ray tracing methodology results in accurate prediction of far field SPL at inclined polar observer angles. The sound-flow interaction effects at different points in the jet flow are studied, and the contribution of sources at different streamwise locations along the jet are examined as a function of emitted frequency.

2 Methodology

2.1 Source model

Ribner's formulation [8] of the Lighthill equation [9] is used as the starting point for acoustic source modeling. The far-field spectrum can then be written as:

$$P(\mathbf{x},\omega) = \frac{1}{(4\pi r)^2}\frac{1}{a_0^3}\bar{\rho}^2 D_f^{-5} d_{ijkl}\int \Phi \mathcal{F}[I_{ijkl}]d^3\mathbf{y}, \tag{1}$$

where $\mathbf{x}$ and $\mathbf{y}$ are respectively the observer and source locations, and $r = |\mathbf{x}|$ is the distance to the far field. a_0 is taken to be the reference speed of sound and $\bar{\rho}$ is the time-averaged flow field density. The Doppler factor D_f is calculated as $1 - M_c\cos(\theta)$. The convective Mach number M_c is defined as:

$$M_c = \frac{1}{4}\left(\frac{U_1}{a}\right) + \frac{1}{3}M, \tag{2}$$

where U_1 is the local time-averaged axial flow speed, a is the local speed of sound, and M is the jet exit Mach number. d_{ijkl} is a tensor accounting for quadrupole directivity. The flow factor Φ, defined below, accounts for flow refraction effects.

$\mathcal{F}[I_{ijkl}]$ denotes the Fourier transform of the fourth order correlation of turbulent velocity fluctuations. We require a model for this tensor quantity:

$$I_{ijkl}(\tau) = \int \frac{\partial^4}{\partial\tau^4}\overline{v_i v_j v_k' v_l'}d^3\xi = \int \frac{\partial^4}{\partial\tau^4}\overline{u_i u_j u_k' u_l'}d^3\xi \tag{3}$$

Here $v_i = U_i + u_i$ is the instantaneous velocity, sum of the mean and fluctuating components. The prime here indicates evaluation at a different spatial and temporal location, separated by $\xi = (\xi_1, \xi_2, \xi_3)$ and τ respectively. Only the fluctuating components of velocity are considered as efficient sources of turbulent mixing noise, allowing the mean components to be dropped. We assume isotropic and locally homogeneous turbulence; it follows that u_i and u_j' are linked by a joint normal probability distribution, allowing the fourth order correlation to be rewritten in terms of second order quantities:

$$\overline{u_i u_j u_k' u_l'} = \overline{u_i u_j}\,\overline{u_k' u_l'} + \overline{u_i u_k'}\;\overline{u_j u_l'} + \overline{u_i u_l'}\;\overline{u_j u_k'}. \tag{4}$$

As $\overline{u_i u_j}$ and $\overline{u_k' u_l'}$ are independent of temporal separation τ, the first of these three terms does not appear in the expression for I_{ijkl}. It then remains to model the second order correlations. We take the form suggested

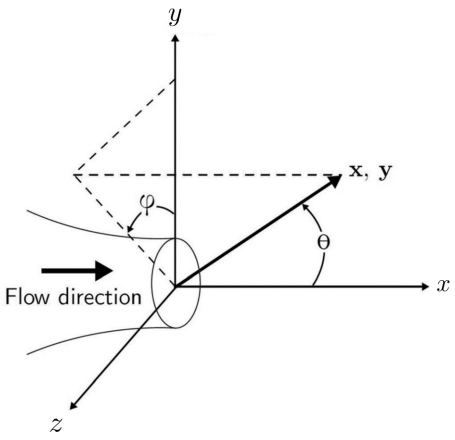

Figure 1: Cartesian and spherical polar coordinate systems.

.

by Ribner [8], in which the spatial and temporal contributions may be considered independently:

$$\overline{u_i u_j'}(\xi,\tau) = R_{ij}(\xi)g(\tau). \tag{5}$$

For homogeneous and isotropic turbulence, the spatial correlation takes the form:

$$R_{ij}(\xi) = \overline{u_1^2}\left[\left(f + \frac{1}{2}|\xi|f'\right) - \frac{1}{2}f'\frac{\xi_i\xi_j}{|\xi|}\right]. \tag{6}$$

Here the prime denotes differentiation with respect to the argument. The function $f(\xi)$ can take many different forms; we choose a Gaussian distribution:

$$f(\xi) = \exp\left(-\pi\frac{\xi^2}{L^2}\right), \tag{7}$$

where L is the characteristic turbulent length scale at the source location. Integrating the fourth order correlation tensor over the spatial source region gives:

$$I(\tau) = \frac{\partial^4 g}{\partial\tau^4}\int (R_{ik}R_{jl} + R_{il}R_{jk})d^3\xi = \frac{\rho}{2\sqrt{2}}k^2L^3\frac{\partial^4 g}{\partial\tau^4}. \tag{8}$$

The index $ijkl$ is dropped from this point to reflect that the modeled sources are isotropic. The effects of far field directivity are accounted for entirely by the Doppler factor, and by the flow factor computed in the next section as a function of observer and source location.

The temporal correlation can also be modeled as a Gaussian:

$$g(\tau) = \exp\left(-\frac{\tau^2}{\tau_0^2}\right), \tag{9}$$

giving the following explicit form for the Fourier transform of the modeled fourth order correlation tensor:

$$I(\Omega) = \frac{\sqrt{\pi}}{4}k^2L^3\tau_0\Omega^4\frac{\sqrt{2\pi}}{2}\exp\left(-\frac{\tau_0^2\Omega^2}{8}\right). \tag{10}$$

Here the modified frequency is given by $\Omega = \omega\sqrt{(1 - M_c\cos\theta)^2 + (\alpha k^{1/2}/a_0)^2}$, where α is an experimental parameter taken to be 0.5. The term $(1 - M_c\cos\theta)$ accounts for the Doppler shift as the source is convected, while the term $(\alpha k^{1/2}/a_0)$ accounts for the finite lifetime of an eddy as it moves downstream.

The characteristic turbulent scales L and τ_0 are calculated from the standard RANS-derived quantities k and ϵ as follows:

$$L = c_l \frac{k^{3/2}}{\epsilon}, \qquad \tau_0 = c_\tau \frac{k}{\epsilon}, \tag{11}$$

where c_l and c_τ are empirical constants. We use the following improved time scale proposed by Azarpeyvand and Self [5] to account for the transfer of turbulent energy between different wavenumbers:

$$\tau_0^* = \tau_0 \left(\frac{L}{D} \right)^{2/3}, \tag{12}$$

where D is the nozzle diameter. This time scale naturally reduces to the conventional scales associated with turbulent production and dissipation in the areas of the jet where these are the dominating noise generation mechanisms. Replacing τ_0 with this improved time scale τ_0^* and substituting into equation 1 gives:

$$I(\Omega) = \frac{\sqrt{\pi}}{4} \frac{c_l^3}{c_\tau^3} k^{7/2} \rho^2 \tau_0^{*4} \Omega^4 \exp\left(-\frac{\tau_0^{*2} \Omega^2}{8} \right). \tag{13}$$

$$\Rightarrow \quad P(\mathbf{x}, \omega) = \frac{1}{64\pi^{3/2}} \frac{1}{r^2 a_0^4} \frac{c_l^3}{c_\tau^3} \int \Phi(\mathbf{x}, \mathbf{y}) D_f^{-5} \rho^2 k^{7/2} \tau_0^{*4} \Omega^4 \exp\left(-\frac{\Omega^2 \tau_0^{*4}}{8} \right) d^3\mathbf{y}. \tag{14}$$

Equation 13 represents the spectrum of the far field sound radiated by a single correlated volume of turbulence within the jet, located at $\mathbf{y}$ and neglecting directivity effects of refraction by the jet flow. These refraction effects are captured by $\Phi(\mathbf{x}, \mathbf{y})$, whose calculation is presented in the next section.

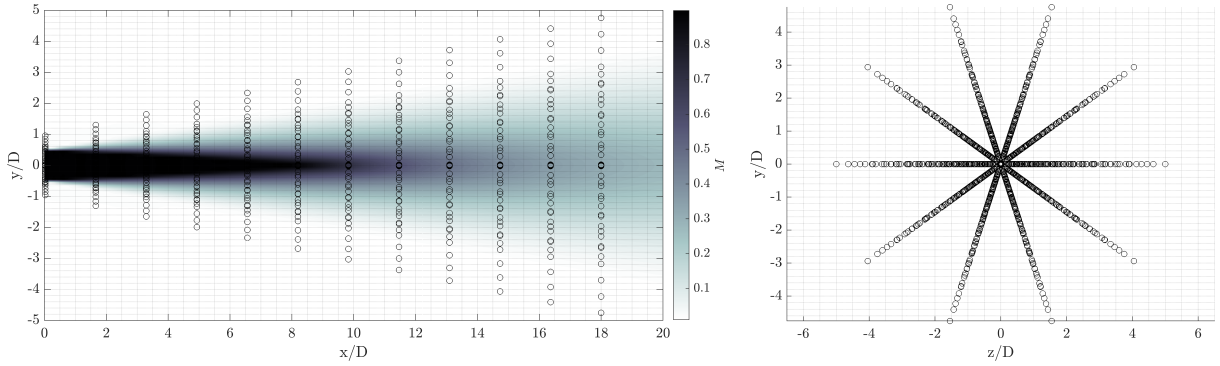

(a) (b)

Figure 2: Source location clustering for ray tracing method.

2.2 Far-field propagation model

The presence of a moving medium and spatial gradients in the speed of sound have a significant effect on the refraction of sound waves reaching the far field. We account for these effects by introducing the flow factor $\Phi(\mathbf{x}, \mathbf{y})$ [7], which represents the ratio of the pressure amplitude measured at location $\mathbf{x}$ due to a source at location $\mathbf{y}$ with and without the jet flow being present. $\Phi(\mathbf{x}, \mathbf{y})$ may be calculated by a number of different methods, such as an adjoint Green's function or asymptotic solution of Lilley's equation. In this work, we make a high frequency approximation in order to make use of the geometrical ray tracing method employed to describe wave propagation in non-uniform media. This method does not require the solution of an additional PDE over a domain extending to the far field, and is well-suited to complex and possibly asymmetric jet configurations.

We follow the ray tracing formulation presented by Pierce [10]. A point x_p^{ray} on the wavefront that defines the position of a ray moves with velocity:

$$\frac{d\mathbf{x}_p^{\text{ray}}}{dt} = \mathbf{v}(\mathbf{x}_p^{\text{ray}}, t) + \mathbf{n}(\mathbf{x}_p^{\text{ray}}, t) a(\mathbf{x}_p^{\text{ray}}, t), \tag{15}$$

where $\mathbf{n}$ is the unit normal vector to the wavefront. To avoid having to construct the full local wavefront surface, we do not work with $\mathbf{n}$ and instead use the wave slowness vector $\mathbf{s}$:

$$\mathbf{s} = \frac{\mathbf{n}}{a + \mathbf{v}.\mathbf{n}}. \tag{16}$$

The ray tracing equations are written in Cartesian coordinates as six coupled ordinary differential equations for the components of ray position and wave slowness:

$$\frac{dx_i^{\text{ray}}}{dt} = U_i + \frac{a^2 s_i}{1 - U_j s_j} \tag{17}$$

$$\frac{ds_i}{dt} = -\frac{1 - U_j s_j}{a}\frac{\partial a}{\partial x_i} - s_j \frac{\partial U_j}{\partial x_i} \tag{18}$$

Equations 17 and 18 are numerically integrated using a fourth-order Runge-Kutta method with a subroutine to interpolate the quantities U_i and a from the RANS simulation data. Each ray is integrated forward in time until it exits the RANS domain - from this point the flow variables are considered to be spatially uniform, and thus the ray follows a straight line to the far field.

The ratio of pressure amplitude at the source and far field locations cannot be determined from the ray tracing solution alone. This ratio can be calculated using the Blokhintsev invariant [11]:

$$\frac{\overline{p^2} V A}{(1 - U_i s_i)\rho a^2} = \text{constant}, \tag{19}$$

where $V = |d\mathbf{x}^{\text{ray}}/dt|$ and A is the ray tube area. Applying equation 19 to a ray that begins at the source location and ends at the observer location gives the following ratio of pressure amplitudes:

$$\frac{\overline{p^2}|_{\mathbf{x}}}{\overline{p^2}|_{\mathbf{y}}} = \frac{\left.\frac{V}{(1-U_i s_i)\rho a^2}\right|_{\mathbf{y}}}{\left.\frac{V}{(1-U_i s_i)\rho a^2}\right|_{\mathbf{x}}} \frac{A|_{\mathbf{y}}}{A|_{\mathbf{x}}} \tag{20}$$

The flow factor that we wish to compute is the ratio of the pressure amplitude in the far field between a ray traced through the jet flow and a ray traced from the same source but through a quiescent medium:

$$\Phi(\mathbf{x}, \mathbf{y}) = \frac{\overline{p^2}|_{\mathbf{x},\text{flow}}}{\overline{p^2}|_{\mathbf{x},\text{quiescent}}} \tag{21}$$

.

In order to calculate Φ from equation 19, we assume that the pressure amplitude and ray tube area at the source itself remains unchanged by the presence of a jet flow, and that for a quiescent flow, the quantity $V/(1-U_i s_i)\rho a^2$ is equal at the source and observer locations. Invoking these assumptions gives the following expression for flow factor:

$$\Phi(\mathbf{x}, \mathbf{y}) = \frac{\left.\frac{V}{(1-U_i s_i)\rho a^2}\right|_{\mathbf{y},\text{flow}}}{\left.\frac{V}{(1-U_i s_i)\rho a^2}\right|_{\mathbf{x},\text{flow}}} \frac{A|_{\mathbf{x},\text{quiescent}}}{A|_{\mathbf{x},\text{flow}}}. \tag{22}$$

As the ray area cannot be found directly from the ray tracing solution, we approximate the ratio of tube areas using ray densities. The far field is represented as a spherical shell discretized into approximately 10^4 equal bins. A large number of rays (approximately 6×10^5 for the results in this paper) are launched from each source location. In order to ensure even coverage over space, the launch angles are chosen to intersect the vertices of a geodesic sphere with a suitably high subdivision frequency. The number of rays intersecting the far field bin closest to the far field location of interest is compared for the ray tracing solution with jet flow (N_{flow}) and without ($N_{\text{quiescent}}$). The flow factor is then calculated as:

$$\Phi(\mathbf{x},\mathbf{y}) = \frac{\left.\frac{V}{(1-U_i s_i)\rho a^2}\right|_{\mathbf{y},\text{flow}}}{\left.\frac{V}{(1-U_i s_i)\rho a^2}\right|_{\mathbf{x},\text{flow}}} \frac{N|_{\mathbf{x},\text{flow}}}{N|_{\mathbf{x},\text{quiescent}}}. \tag{23}$$

$\Phi(\mathbf{x},\mathbf{y})$ is calculated for each of the finite number of source locations (approximately 10^3 for the results in this paper). The sources are non-uniformly distributed through the jet flow, with the highest density of source placement in areas of high velocity gradient and turbulent kinetic energy as in figure 2.

The acoustic source and ray tracing codes are implemented using Jax [12], an Autograd-supported framework that allows automatic differentiation of native Python code. In our intended further work, this will allow us to extract sensitivities which may be coupled with a RANS CFD adjoint as discussed in section 4. Automatic differentiation is already integrated into the SU2 code used for the RANS computation.

3 Results

3.1 RANS mean flow solution

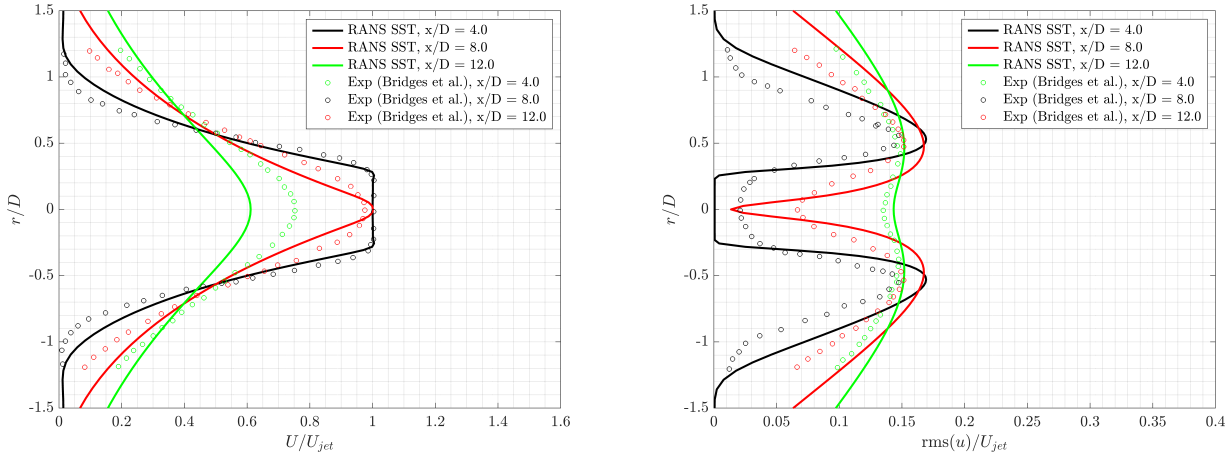

(a) (b)

Figure 3: Comparison of (a) mean flow velocity and (b) rms velocity fluctuations against experimental data for three streamwise locations.

In this work, we study an isothermal turbulent round jet at a jet Mach number of $M_j = 0.9$. The Reynolds number based on the nozzle diameter of $D = 0.06223m$ is $Re_D = 1.1 \times 10^6$. This test case was previously studied in the context of the EU Project Go4Hybrid (G4H) and simulated with hybrid RANS/LES methods [13]. Three meshes used in the project, ranging from 1.6M cells (G1) to 8.8M cells (G3), were graciously shared by the G4H partners. The mean flow simulation in the present study is performed using the open source $SU2$ code [14]. The finite volume method is applied on arbitrary unstructured meshes using a standard edge-based data structure with control volumes constructed using a median-dual, vertex-based scheme. The continuity, momentum and energy equations for a compressible gas are solved together with the ideal gas equation of state. The standard $k-\omega$ model is used, with the two additional equations governing the turbulent quantities solved using the standard coefficient values.

The simulation results are compared against experimental data from Bridges and Wernet [15] in Figure 3. The mean flow velocity profile is captured with relatively high accuracy at short distances downstream of the nozzle exit. Further downstream, the G1 mesh becomes significantly coarser, resulting in much greater discrepancy between the computed and measured mean flow velocities. The rms velocity fluctuations (estimated by rescaling the computed turbulent kinetic energy) similarly follows approximately the correct profile shape but is not very accurate when compared against experiment. However, it should be noted that

even these approximately correct RANS solutions from a relatively coarse mesh are capable of producing good noise predictions, as discussed in 3.4, suggesting that the acoustic prediction methodology is relatively robust to minor inaccuracies in the base flow RANS simulation.

3.2 Source location results

The source model developed in section 2.1 gives an expression for the spectrum of radiated sound associated with each correlated volume element in the jet flow. We may use this to study in more detail how sound sources are spatially distributed within the jet plume. This distribution sheds light on both the mechanisms by which the noise is produced and radiated, and also points to how jet noise reduction technologies should aim to alter the flow field. For this purpose, the volume integral in equation 14 is computed over slices in the $y-z$ plane, to obtain the far-field noise contribution at a particular frequency as a function of downstream axial location.

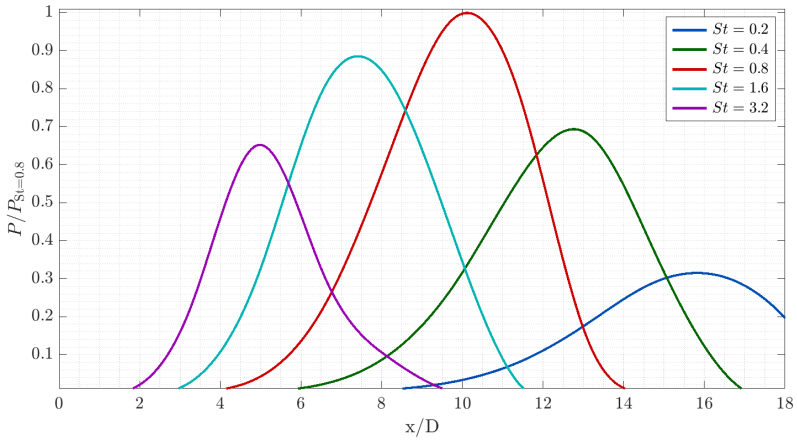

Figure 4: Source distribution as a function of axial distance for different Strouhal numbers, normalized by the maximum of the distribution for $St = 0.8$.

Figure 4 shows the source distributions for an observer located at $\theta = 90^o$, for five different Strouhal numbers. The source distribution amplitudes are normalized by the amplitude at St = 0.8. As physically expected, the results indicate that lower frequency sources are located further downstream; these sources are associated with large eddy structures, which are mostly formed close to the jet axis and in the region where the flow is fully developed. Meanwhile, high frequency sources are quite close to the nozzle exit, where the shear layer is still relatively thin. The most energetic sources appear to be clustered just downstream of the end of the jet's inviscid core (located at approximately $x/D = 9$ from the RANS simulation); this is accounting for the over-prediction of the potential core length that is well known to arise when using the standard $k-\epsilon$ turbulence model.

3.3 Sound-flow interaction effects

The purpose of the ray-tracing model for far-field propagation is to capture sound refraction due to interaction between the flow field and the acoustic waves. These effects can be observed in the paths taken by the rays between the source locations and the far field. In the absence of any flow, and any flow gradients, each ray would follow a straight line from its source to its observer location on our chosen far field sphere following the angle at which it was launched. When the jet flow is included, there is a high degree of ray curvature in regions with high spatial gradients of velocity and sound speed. The flow factor is calculated by comparing the number of rays that end at a given far field location for the cases of no flow (straight rays) and jet flow (curved rays).

Figure 5 shows the paths taken by a small number of rays being launched from an example source located close to the jet axis and to the end of the potential core. Some of the rays cross through the shear layer

region, where velocity and speed of sound gradients along the ray paths are high. This has the effect of curving these rays away from the jet axis. Based on this observation, we expect that the addition of the flow factor will, in the case of acute polar observer angles, decrease the far-field SPL as compared to that obtained using the source model alone. Conversely, in the case of obtuse polar angles, we expect to see the SPL increased by flow refraction effects. At an observer angle of 90^o, the effects of refraction due to sound-flow interaction should be very small; therefore it is physically expected that the flow factor should be close to unity for all source locations.

It should also be noted that rays launched from this source location that fall within a critical range of launch angles remain trapped inside the jet's potential core. This behavior is physically expected - the rays undergo total internal reflection upon encountering a critically high value of local flow gradient transverse to the shear layer. The trapping of these rays and the corresponding reduction in effective acoustic propagation from inside this region to the far field leads to the conclusion that there is no significant concentration of true acoustic sources in the inviscid core. In choosing the locations for the fictional sources in the ray tracing method, it is therefore inefficient to place a very large number of sources inside this core.

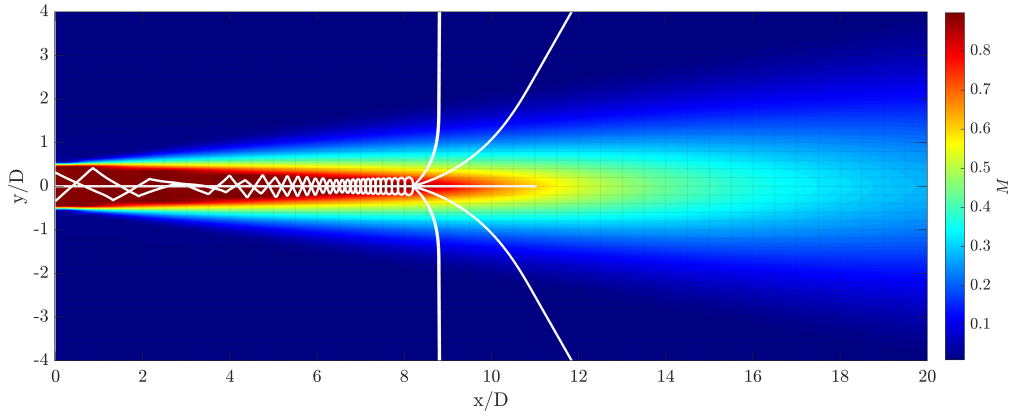

Figure 5: Ray paths (white) curved due to flow refraction effects.

The effects of refraction on the computed far-field SPL may be studied in isolation by plotting the flow factor $\Phi(\mathbf{x}, \mathbf{y})$ as a function of source location $\mathbf{y}$ for different values of the polar observer angle. $\Phi(\mathbf{x}, \mathbf{y})$ gives the factor by which the SPL due to noise propagating from location $\mathbf{y}$ and received at location $\mathbf{x}$ is amplified due to sound-flow interaction effects. The flow factor is plotted in Figure 6 on a decibel scale ($10\log(\Phi)$) for polar angles of 90^o and 60^o (with the azimuthal observer angle fixed at 90^o) to demonstrate the net effect of ray curvature for sources in different regions of the jet plume. Positive values indicate refractive amplification, while negative values correspond to attenuation. It can be seen that for an observer located at $\theta = 90^o$, the flow factor value is everywhere close to one as expected; amplification due to refraction is negligible. At acute polar angles, however, in regions close to the nozzle exit where velocity and sound speed gradients are significant, there are large shifts due to the effects of sound-flow interaction. Much of the acoustic source region is attenuated, most significantly in the inviscid core where total internal reflection is a dominating effect as previously discussed. It should also be noted that the flow factor distribution is not axisymmetric, even for this axisymmetric round jet case. Ilario et al. [7] demonstrated that sources located on the opposite side of the jet to the observer location of interest are subject to the greatest refraction shift. This is consistent with our observation of high ray curvature coincident with traversing the shear layer. Sources located opposite the observer must pass through these high gradient regions twice before reaching the far field, resulting in a higher degree of ray scattering.

3.4 Far-field noise predictions

In order to relate the RANS-derived turbulent quantities k and ϵ to the length and time scales relevant to the noise generation process, empirically calibrated coefficients appearing in the source model must be chosen. In contrast to many other RANS-based acoustic prediction methods, which require three coefficients (corresponding to amplitude, length scale and time scale), the source model implemented in the present

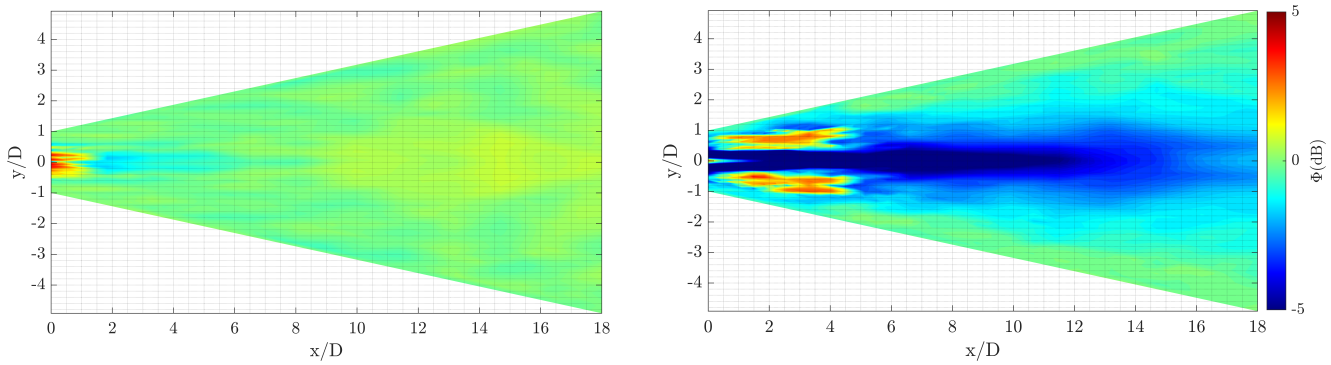

(a) (b)

Figure 6: Flow factor for observer angles of (a) $\theta = 90^o$ and (b) $\theta = 60^o$. Observer above plane of figure ($\phi = 90^o$).

study requires only two coefficients, c_l and c_τ. Previous studies have demonstrated that these coefficients are both relatively independent of the operating Mach number; however, c_l exhibits a strong dependence on the jet temperature ratio [7]. In order to avoid the need to recalibrate the c_l value for heated jet cases, the source model may be extended to include additional source terms relevant to hot jets, such as variable density. In this work, the values of the two coefficients are chosen by comparing the computed SPL for a 90^o polar observer angle, using the source model in isolation, against experimental measurements; the values chosen in this study are $c_l = 7.5$ and $c_\tau = 1.4$.

Figure 7 shows a comparison of computed SPL against experimental data for three different polar observer angles. The predictions compare very favorably in terms of both peak frequency location and the overall spectrum shape, indicating that the physical mechanisms of noise generation are well captured by the source model. Refraction has a very significant effect for observer angles away from 90^o, as demonstrated by the large spectrum shifts embedded in the flow factor.

4 Summary and Future Work

In this work, we have implemented a hybrid RANS-based acoustic prediction tool, consisting of an acoustic source model based on Ribner's formulation of Lighthill's acoustic analogy, coupled with a far field propagation model based on a geometrical acoustics method. We use an SST RANS simulation performed using the SU2 code as input to the prediction tool to compute the far field SPL at three different polar observer angles. The resulting far field spectra compare favorably with experimental data at all three observer locations, demonstrating that this type of hybrid prediction methodology provides a reliable and computationally affordable alternative to acoustic prediction methods requiring expensive unsteady simulations such as LES or DNS. Our implementation of the source and propagation models as separate modules allows us to study their effects in isolation. Computation of the spatial distribution of the flow factor allows us to capture the effects of mean flow sound refraction, and studying the source distribution integrated over streamwise flow 'slices' allows us to observe which portions of the jet contribute most strongly to different frequency ranges in the spectrum.

In future work, we will extend our implementation of the acoustic prediction tool to include algorithmic differentiation, allowing us to obtain gradients of far field SPL with respect to base flow variables in a computationally affordable manner. Integrating such an AD-enabled implementation with the existing discrete adjoint framework in SU2 will allow us to cheaply compute optimization gradients for design parameters chosen to describe the nozzle configuration. This framework will in turn allow low-cost automated shape optimization of nozzles for jet noise minimization under various operating conditions. Integration of our geometrical acoustic method with the SU2 platform will allow us to leverage existing tools for automated design optimization, such as mesh deformation routines and automated parameterization using free form deformation. One aspect we are particularly interested in exploring is the effect of parameterization choice

on the final design shape and performance - for example, the differences achieved by using a small number of explicit parameters, a fully non-symmetric freeform design, or a freeform deformation of individual nozzle sectors while enforcing overall rotational symmetry.

5 Acknowledgements

The first author gratefully acknowledges the financial support of the FAA under Project 59 ('Multifidelity modeling for supersonic aircraft exhaust noise'). Some of the computing for this project was performed on the Sherlock cluster. The authors would like to thank Stanford University and the Stanford Research Computing Center for providing computational resources and support that contributed to these research results.

References

[1] Thomas F. Balsa and Philip R. Gliebe. Aerodynamics and noise of coaxial jets. *AIAA Journal*, 15(11):1550–1558, 1977.

[2] Abbas Khavaran, Eugene A. Krejsa, and Chan M. Kim. Computation of supersonic jet mixing noise for an axisymmetric cd nozzle using k-epsilon turbulence model. 1992.

[3] C. Tam and Laurent Auriault. Jet mixing noise from fine-scale turbulence. 1998.

[4] Philip J. Morris and F. Farassat. Acoustic analogy and alternative theories for jet noise prediction. *AIAA Journal*, 40(4):671–680, 2002.

[5] M. Azarpeyvand and R. H. Self. Improved jet noise modeling using a new time-scale. *The Journal of the Acoustical Society of America*, 126(3):1015–1025, 2009.

[6] Rod H. Self and Mahdi Azarpeyvand. Jet noise prediction using different turbulent scales. *Acoustical Physics*, 55(3):433–440, May 2009.

[7] Carlos R. S. Ilário, Mahdi Azarpeyvand, Victor Rosa, Rod H. Self, and Júlio R. Meneghini. Prediction of jet mixing noise with lighthill's acoustic analogy and geometrical acoustics. *The Journal of the Acoustical Society of America*, 141(2):1203–1213, 2017.

[8] H. S. Ribner. Quadrupole correlations governing the pattern of jet noise. *Journal of Fluid Mechanics*, 38(1):1–24, 1969.

[9] Michael James Lighthill and Maxwell Herman Alexander Newman. On sound generated aerodynamically i. general theory. *Proceedings of the Royal Society of London. Series A. Mathematical and Physical Sciences*, 211(1107):564–587, 1952.

[10] A.D. Pierce. *Acoustics – An Introduction to its physical principles and applications.* Acoustical Society of America, 1991.

[11] D. Blokhintsev. The propagation of sound in an inhomogeneous and moving medium. *Journal of the Acoustical Society of America*, 18(2):322–328, 1946.

[12] James Bradbury, Roy Frostig, Peter Hawkins, Matthew James Johnson, Chris Leary, Dougal Maclaurin, George Necula, Adam Paszke, Jake VanderPlas, Skye Wanderman-Milne, and Qiao Zhang. JAX: composable transformations of Python+NumPy programs, 2018.

[13] M. Fuchs, C. Mockett, M. Shur, M. Strelets, and J. C. Kok. Single-stream round jet at m = 0.9. In Charles Mockett, Werner Haase, and Dieter Schwamborn, editors, *Go4Hybrid: Grey Area Mitigation for Hybrid RANS-LES Methods*, pages 125–137, Cham, 2018. Springer International Publishing.

[14] Thomas D. Economon, Francisco Palacios, Sean R. Copeland, Trent W. Lukaczyk, and Juan J. Alonso. Su2: An open-source suite for multiphysics simulation and design. *AIAA Journal*, 54(3):828–846, 2015.

[15] J. Bridges and M. Wernet. Establishing consensus turbulence statistics for hot subsonic jets. AIAA-2010-3751, 2010.

(a)

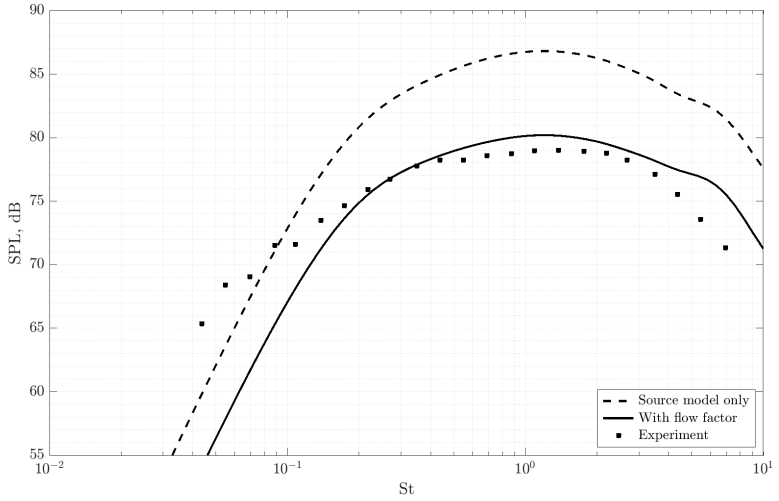

(b)

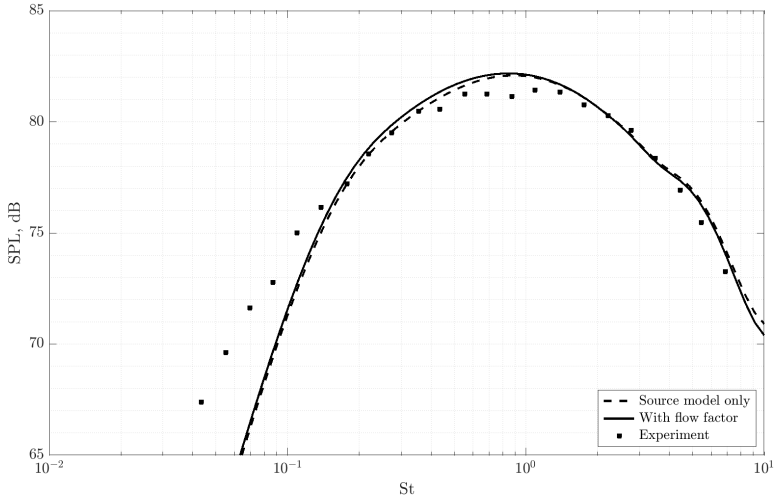

(c)

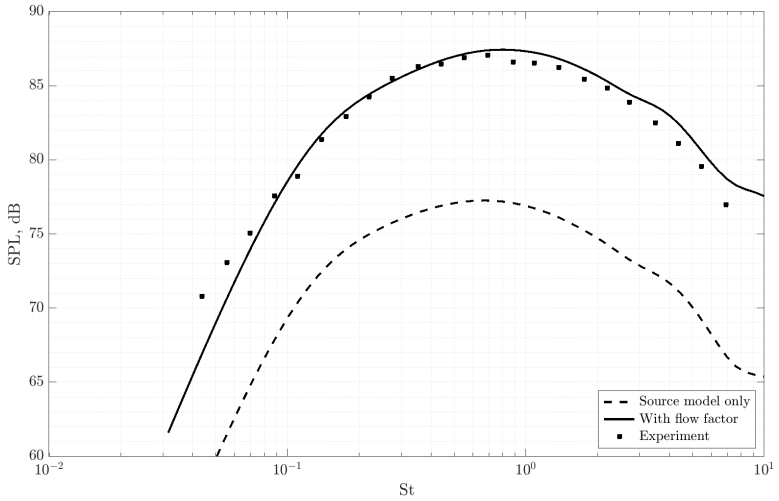

Figure 7: Far field SPL predictions at (a) $\theta = 60^o$, (b) $\theta = 90^o$ and (c) $\theta = 130^o$ compared against experimental data, with and without flow refraction effects taken into account.